

Transmission and absorption of solar radiation by Arctic sea ice during the melt season

Bonnie Light,¹ Thomas C. Grenfell,² and Donald K. Perovich³

Received 17 October 2006; revised 1 June 2007; accepted 5 November 2007; published 21 March 2008.

[1] The partitioning of incident solar radiation between sea ice, ocean, and atmosphere strongly affects the Arctic energy balance during summer. In addition to spectral albedo of the ice surface, transmission of solar radiation through the ice is critical for assessing heat and mass balances of sea ice. Observations of spectral irradiance profiles within and transmittance through ice in the Beaufort Sea during the summer of 1998 during the Surface Heat Budget of the Arctic Ocean (SHEBA) are presented. Sites representative of melting multiyear and first-year ice, along with ponded ice were measured. Observed spectral irradiance extinction coefficients (K_λ) show broad minima near 500 nm and strong increases at near-infrared wavelengths. The median K_λ at 600 nm for the bare ice cases is close to 0.8 m^{-1} and about 0.6 m^{-1} for ponded ice. Values are considerably smaller than the previously accepted value of 1.5 m^{-1} . Radiative transfer models were used to analyze the observations and obtain inherent optical properties of the ice. Derived scattering coefficients range from 500 m^{-1} to 1100 m^{-1} in the surface layer and 8 to 30 m^{-1} in the ice interior. While ponded ice is known to transmit a significant amount of shortwave radiation to the ocean, the irradiance transmitted through bare, melting ice is also shown to be significant. The findings of this study predict 3–10 times more solar radiation penetrating the ice cover than predicted by a current GCM (CCSM3) parameterization, depending on ice thickness, pond coverage, stage of the melt season, and specific vertical scattering coefficient profile.

Citation: Light, B., T. C. Grenfell, and D. K. Perovich (2008), Transmission and absorption of solar radiation by Arctic sea ice during the melt season, *J. Geophys. Res.*, 113, C03023, doi:10.1029/2006JC003977.

1. Introduction

[2] The extent and total mass of the Arctic multiyear sea ice pack are potentially sensitive indicators of climate change that vary in response to changes in heat fluxes at the top, bottom, and lateral boundaries of the pack over an annual cycle. A critical stage in this cycle is the melt season whose intensity and duration are central in determining the heat and mass balance of the ice cover. The melt season is primarily driven by solar radiation that strongly affects the ablation of the ice at its upper and lower surfaces, lateral melting of floe edges, the formation and development of melt ponds, and internal storage of latent heat by inclusions of liquid brine. At visible wavelengths in particular, solar radiation is also critical for biological processes that occur within the ice and in the underlying ocean.

[3] Scattering and absorption by snow and ice determine the spatial and temporal distribution of solar heating in the

atmosphere-ice-ocean system. This critical aspect of the heat and mass balance can produce positive feedbacks between ice extent, ice thickness, and regional climate. It is an active topic of current experimental research and theoretical modeling at regional, basin, and global scales [Ebert and Curry, 1993; Curry *et al.*, 1995; Moritz and Perovich, 1996; Holland *et al.*, 1997; Bitz *et al.*, 2001; Holland *et al.*, 2006]. The ramifications of interactions between solar radiation and the ice cover for the Arctic Basin and global climate are beginning to be addressed, but accurate descriptions of the radiative and physical processes involved are still under development. The partitioning of radiation between ice, ocean, and atmosphere is also of central importance for the arctic marine ecosystem [e.g., Perovich *et al.*, 1993; Comiso *et al.*, 2003]. Large-scale model simulations [Walsh *et al.*, 2004] suggest that sea ice changes and associated alterations in biodiversity are likely to be key components altering Arctic marine food web structure and function over the next decades.

[4] For the past 30 years there has been a persistent decrease in summer minimum ice extent of about 7.7% per decade [Parkinson *et al.*, 1999; Parkinson and Cavalieri, 2002; Cavalieri *et al.*, 2003]. Extreme summer retreat of the ice pack in 2002 through 2005 [Stroeve *et al.*, 2005] indicates the possibility of an accelerating decrease. This demonstrates that an understanding of the large-scale mass balance of multiyear ice needs to take into account situations where the

¹Applied Physics Laboratory, Polar Science Center, University of Washington, Seattle, Washington, USA.

²Department of Atmospheric Sciences, University of Washington, Seattle, Washington, USA.

³Cold Regions Research and Engineering Laboratory, Engineer Research and Development Center, Hanover, New Hampshire, USA.

ice thickness becomes very small or the ice melts altogether. Recent submarine sonar observations [Rothrock *et al.*, 1999] showing a significant decrease in mean multiyear ice thickness underscore the importance of this question.

[5] To understand the role of solar radiation in quantitative detail, an understanding of the transmission of solar radiation through the ice is needed in addition to the spectral albedo, particularly for bare and ponded summer ice. For example, Hayes [2003] found that to explain the oceanic heat flux required to account for the observed bottom ablation of multiyear ice during the SHEBA experiment, it was necessary to include the shortwave radiation transmitted directly through the ice and deposited in the upper ocean. Similarly, Perovich [2005] estimated that light penetration through bare and ponded ice accounted for 23% and 16% of the solar energy input to the ocean, respectively. In a climate regime exhibiting reduced mean sea ice thickness, an accurate understanding of the role of shortwave radiation transport into and through the ice cover is crucial for ice models over all spatial scales.

[6] Considerable effort has been devoted to understanding the temporal development of the albedo of various surface types, particularly over the summer melt season [Grenfell and Perovich, 1984; Perovich, 1994; Grenfell *et al.*, 1998; Pegau and Paulson, 2001; Hanesiak *et al.*, 2001; Perovich *et al.*, 2002; Grenfell and Perovich, 2004]. An important result emerging from these studies is that once the snow cover has melted, the albedo of melting bare sea ice is approximately independent of time and the temporal variations in regional albedo are driven largely by changes in the amount of open water and the areal coverage and optical properties of melt ponds. This provides the basis for a physical model of regional albedo [Perovich, 1990; Eicken *et al.*, 2004], but the more general question of partitioning requires additional information about the optical properties of the interior of the ice.

2. Previous Work

[7] Several observational and theoretical investigations of the solar radiation transmittance for sea ice have been carried out to date. On the basis of changes in the vertical temperature profile in the ice, Untersteiner [1961] estimated broadband irradiance extinction coefficients of 1.5 m^{-1} for thick multiyear ice. Owing to the strong wavelength dependence of the absorption and irradiance extinction coefficients of sea ice, spectral observations are required for an accurate determination of the partitioning of the radiation. Grenfell and Maykut [1977] reported spectral albedos and vertically averaged irradiance extinction coefficients for melting bare ice, blue ice, and melt ponds at selected sites on first-year (FY) and multiyear (MY) ice, corroborating and extending Untersteiner's observations.

[8] Field observations of transmittance have been reported for selected sites and ice types [Grenfell and Maykut, 1977; Perovich *et al.*, 1993; Mobley *et al.*, 1998; Perovich *et al.*, 1998a, 1998b; Pegau and Zaneveld, 2000]. Perovich and Grenfell [1981] used slabs of laboratory-grown sea ice to estimate the temperature-dependence of spectral transmittance and the irradiance extinction coefficient for newly grown, thin ice. These studies have provided substantial insight into the inherent optical properties of the

interior ice and have shown the importance of the vertical layer structure as well as the role of biological and inorganic inclusions in modulating the absorption of radiation. During the summer melt season, however, when the radiation partitioning has its largest impact, the sea ice cover is rarely composed of horizontally homogeneous ice that can be neatly parsed into area-weighted averages. Rather, it consists of a mixture of snow covered, bare, and ponded ice typically varying on 1 to 10 m horizontal scales. Such a horizontally inhomogeneous domain yields backscattered, absorbed, and transmitted radiation fields whose spatial distribution reflects the complexity of the physical variations in the ice cover [Perovich, 1991].

[9] Numerical models for simulating the transport of radiation by sea ice and snow span a wide range of sophistication. Comparisons with field observations have been generally good but are limited by a scarcity of high-quality radiation data and a limited knowledge of the vertical structure and impurity content of the ice and snow. Early models employed a Beer's law representation [Grenfell and Maykut, 1977] or an upwelling and downwelling irradiance calculation [Grenfell, 1979; Perovich, 1991, 1994] to estimate the attenuation of solar radiation in the ice and snow, but these required specification of inherent optical properties (IOPs) of the system that could not be related directly to the physical structure of the ice. These radiative transfer models are limited by the requirement of ad hoc IOP values to account for variations in absorption and scattering.

[10] More precise discrete ordinate models have been developed in conjunction with IOP models of the ice and snow [Perovich and Grenfell, 1981; Grenfell, 1983, 1991; Grenfell *et al.*, 1994; Jin *et al.*, 1994; Light *et al.*, 2004]. The effects of foreign inclusions in the ice and snow have also been addressed [Clarke and Noone, 1985; Light *et al.*, 1998; Grenfell *et al.*, 2002]. These models couple the physical properties with the IOPs of the ice and allow a general representation of vertical layer structure; however, they are one-dimensional and thus require each surface type have large horizontal extent over which the structure is uniform. Accounting for horizontal variability is important, for example, for the influence of bare ice on the transmitted irradiance through adjacent melt ponds and visa versa. The influence of boreholes required for transmittance measurements must also be properly taken into account.

[11] Theoretical studies investigating the regional deposition of shortwave radiation within sea ice have been carried out by Perovich [1990, 1991, 2005] and Ebert *et al.* [1995]. These modeling results are useful for applying existing optical data to investigate detailed partitioning of shortwave radiation in a column model, and they underscore the importance of spatial inhomogeneities in the summer ice cover. They are limited, however, because the results are based on IOPs that assume a simplified model for the vertical variations in the optical properties of the ice column and do not account for spatial and temporal variability in sufficient detail.

[12] In this paper we present a study of spectral transmittance observed within and under sea ice in the Beaufort Sea over the 1998 summer melt season during the SHEBA experiment [Perovich *et al.*, 1999; Uttal *et al.*, 2002]. The data set has been presented by Grenfell *et al.* [2006], but the treatment presented in this paper offers considerably more detail and analysis. The results are used in conjunction with

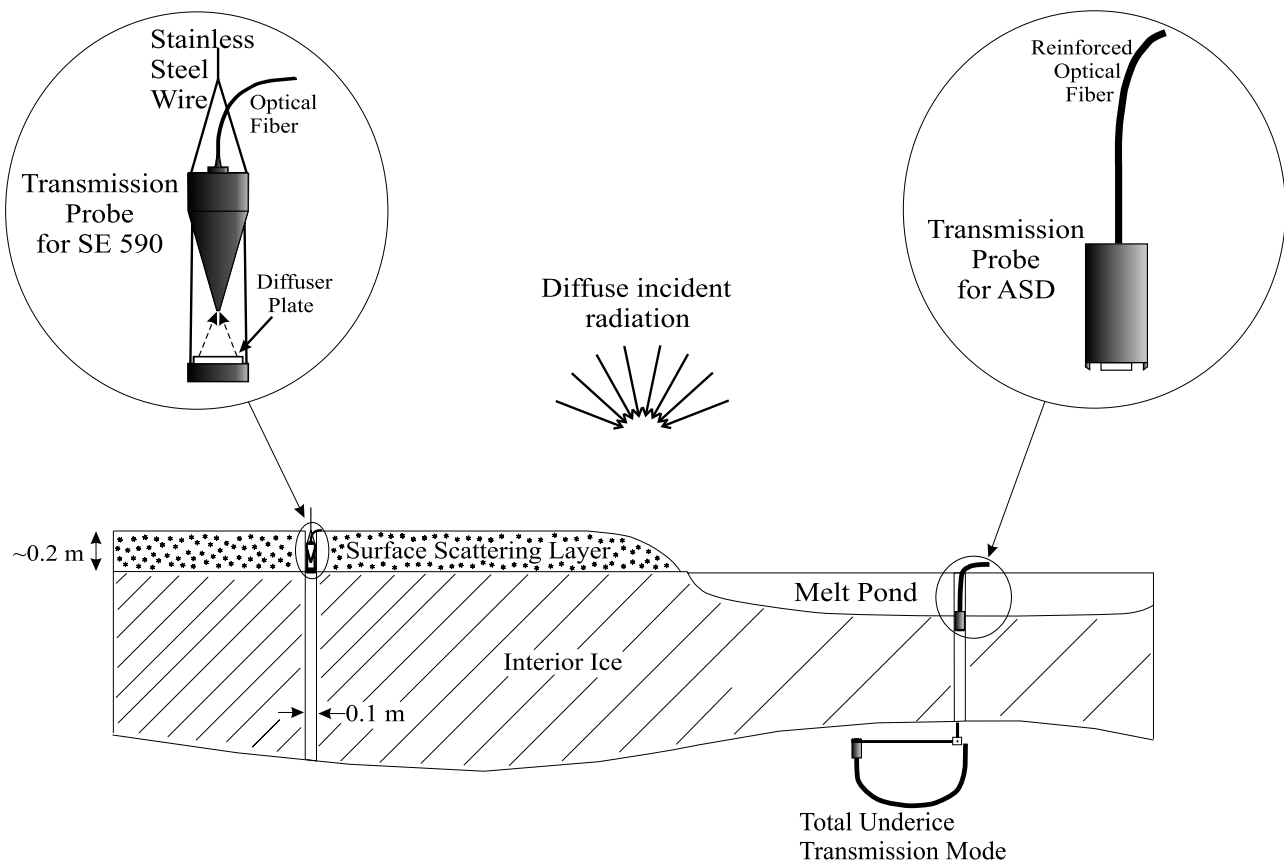


Figure 1. Transmission probes for SE 590 and ASD spectrophotometers. An irradiance receptor was connected to the spectrophotometer by a 10 m long fiber. Each probe was lowered in 0.05–0.10 m increments down a bore hole and into the water to record downward propagating and upward propagating radiation. Spectral transmittance was measured with the ASD probe using an extension arm to position the sensor in upward looking orientation 1.5 m away from the bore hole.

high resolution spectral albedo observations and with radiative transfer model analysis to characterize the depth dependence and variability of the optical properties of the ice cover.

3. Approach and Instrumentation

[13] The advent of new high-resolution diode-array spectrophotometers with significantly improved sensitivity, spectral resolution, reliability, and recording speed has made possible greatly improved measurements of the apparent optical properties (AOPs) of the sea ice cover. Improvements in optical fiber technology have also made in-ice and underice observations of light fields much easier, substantially improving their accuracy.

[14] In this study, two types of transmission measurement were carried out: (1) spectral transmittance was estimated using measurements of downwelling irradiance at the surface and the underside of the ice, and (2) vertical profiles of downwelling and upwelling irradiance were measured at approximately every 0.10 m within boreholes in both bare and ponded ice. Two separate spectrophotometers were used, a Spectron Engineering SE 590 for downwelling irradiance (wavelength coverage 400–1000 nm) and an Analytical Spectral Devices ASD Ice-1 dual channel instrument for both upwelling radiation and transmittance (wave-

length coverage 400–890 nm). Both instruments (Figure 1) were equipped with 10-m optical fibers with irradiance receptors. Because of the strong attenuation of red and near-infrared radiation by snow and ice, the useful range of transmitted light was limited to 400–700 nm. The spectral resolution was 2–4 nm, depending on instrument and wavelength.

[15] A full set of optical measurements included spectral albedos, vertical profiles of upwelling and downwelling irradiance, and under-ice transmittance. Spectral albedo was measured at the surface of each site at ultraviolet, visible, and near infrared wavelengths covering the spectral range 320 to 1800 nm [Perovich *et al.*, 2002]. A custom-built integrating sphere was mounted directly on the SE590 recording head on the end of a 1.5 m arm supported by a tripod. The integrating sphere was tested and shown to have a sufficiently accurate cosine response [Perovich *et al.*, 2002]. The head was oriented to look upward and then at the surface, taking both readings within a 10–15 s interval, and averages of multiple readings were obtained to reduce uncertainties due to unstable illumination conditions as much as possible.

[16] Vertical profiles of downwelling irradiance within the ice were measured using a profiler equipped with an upward looking receptor. The profiler consisted of an optical fiber probe aimed at a diffusely reflecting Spectralon

target. The instrument housing caused a 15 degree cone to be blocked such that light coming directly down the borehole was not recorded. Variations in the incident illumination were monitored to take into account temporal changes in the radiation field during each profile. Near the surface, the downwelling radiation was perturbed by the discontinuity caused by the borehole itself. Deeper in the ice, radiation disturbed by the borehole filled a decreasing fraction of the instrument field of view. A two-dimensional radiative transfer model [Light *et al.*, 2003a] was used to evaluate the significance of these effects (see section 7).

[17] Observations of spectral transmittance were made by recording downwelling irradiance below the ice by lowering an irradiance receptor mounted to the end of a 2-m hinged arm down a 0.10 m diameter bore hole through the ice. The detector was coupled to a fiber optic cable that was connected to a spectrophotometer at the surface. The lower portion of the arm was hinged and equipped with floatation so that the sensor rotated into position looking upward about one meter away from the hole.

[18] Observations using these instruments were made on an ad hoc basis as conditions allowed during June, July, and August when melt rates were high and the impact of ice-albedo feedback was large. Although this was not a detailed time series, it provided an array of case studies at selected sites over the course of the melt season. Sites were located where the ice cover appeared to be as horizontally homogeneous as possible. At each site, an ice core was taken and photographed to record the vertical layering of the ice structure.

[19] Simultaneous physical property observations were carried out including total ice thickness, pond or snow depth as applicable, freeboard depth, and the thickness and character of obviously distinguishable layers within the uppermost 0.2 to 0.5 m of the ice. Generally, the most prominent layer was the “surface scattering layer” (SSL). This layer typically formed on all areas of melting ice and was manifested as an easily observable bright white layer at the ice surface with a crumbly texture. Typically, the SSL had thickness 0.01–0.1 m and was underlain by another highly scattering layer intermediate between the SSL and the more translucent interior ice. This intermediate layer will be referred to as the “drained layer” (DL) and it typically appeared slightly less bright than the SSL.

4. Observational Data

[20] Observational sites were chosen in areas where the surface conditions appeared typical of the broader region. Adjacent bare ice and ponded ice sites were typically measured together whenever possible. This served to provide a look at the interior ice for areas with high surface albedo in contrast to the interior ice in areas with low surface albedo. Sites were not periodically revisited, but new sites established each time a profiling measurement was made. This avoided the disturbances involved with the sampling activities and made it possible to obtain data on a wide variety of ice types and pond conditions.

[21] Six sites on melting summer MY ice distributed throughout the melt season were determined to be representative: (1) 6–9 July, (2) 21 July, (3) 27 July, (4) 6 August, (5) 23 August, and (6) 3 September. Four additional cases of

particular interest are also presented: 14 July (clean and sediment-laden MY ice) and first-year ice on 26 June and 15 August. Figure 2 shows site photos for each location.

[22] Spectral irradiance extinction coefficients (K_λ) were derived from the irradiance profiles between two depths, z_1 and z_2 , using the finite-difference formula:

$$K_\lambda(z) = \frac{-2}{[F_\lambda(z_2) + F_\lambda(z_1)]} \frac{F_\lambda(z_2) - F_\lambda(z_1)}{(z_2 - z_1)} \quad (1)$$

where $z = [z_1 + z_2]/2$ and F_λ is the downwelling irradiance at wavelength λ . Similarly, equation (1) can be used to describe an upwelling extinction coefficient by supplying upwelling irradiance values for F_λ . Equation (1) is the exact result in the limit of very thin layers and in cases where the irradiance profile is logarithmic. K_λ depends on the scattering and absorption in the domain, as well as the nature of the incident light field (direct or diffuse fields) and the boundary conditions of the domain. Observations were generally used from the depths of 0.35 m and 0.75 m in order to avoid complications introduced by measurements closer to the surface, which would be affected by lateral variations caused by the presence of the bore hole cut for the profiler. Also, the solar radiation transmitted through adjacent melt ponds was observed to modify the radiation field in the deeper layers directly beneath bare ice. For these circumstances, the light leaking in from neighboring ponds may cause ambiguity in the estimation of irradiance extinction coefficients and inferred scattering coefficients at depth. Visual examination of ice cores indicates that in general the structure and texture of the ice at depth does not vary strongly unless bubble layers or foreign inclusions are present.

4.1. Bare and Melting Multiyear Ice

[23] Observations were carried out on bare, melting multiyear ice on 6 and 9 July, 21 July, 27 July, 6 August, 23 August, and 3 September. The 6 and 9 July measurements were made in separate boreholes at approximately the same location. The 6–9 July site along with the 21 July and 27 July sites were characterized as level, bare, melting MY ice. As of July, the melt season was well established and these results are felt to be representative of the early stages of melt. The 6 August site was taken near the maximum areal fraction of ponded ice of 24% [Perovich *et al.*, 2002]. The 23 August site was on the flank of an old multiyear ridge. In this case the ice thickness exceeded 2.5 m, and the bore hole did not penetrate completely through the ice. Observations on 3 September provide data during the initial stages of fall freeze-up. Details about the ice thickness, vertical layer structure, and incident light conditions are given in Table 1.

[24] Spectral albedos (α_λ) for the six bare, melting MY ice cases are shown in Figure 3a. Bare ice albedos show maximum values of 0.80 around 500 nm. The albedos on 23 August and 3 September were slightly larger than at the other bare ice sites, due to a dusting of new snow. The 21 July albedo appears low likely because of reduced scattering at the immediate surface of the ice. The July–August average bare ice albedo measured along the “albedo line” is shown for comparison [Perovich *et al.*, 2002]. Examples of upwelling and downwelling irradiance profiles are shown



Figure 2. Selected site photographs. Some images show the bare ice site and some show the ponded ice site. Image from 17 July is a photograph of a core extracted from bare, melting multiyear ice. While this core was not associated with optical measurements, it appears representative of the ice during the height of melt. Annotations indicate the approximate extent of the surface scattering layer (SSL), drained layer (DL), and interior ice.

Table 1. Physical Property Data and Incident Light Conditions for Each of the Bare and Pondered Multiyear Cases Studied

Date	Stage of Melt	Snow Cover (m)	Surface Scattering Layer Thickness (m)	Freeboard (m)	Bare Ice Thickness (m)	Thickness of New Ice on Pond (m)	Pond Depth (m)	Pondered Ice Thickness (m)	Incident Light Conditions
6, 9 Jul	early	none	0.045	0.22	1.42	none	0.24	1.84	partial overcast
21 Jul	early	none	0.03	0.38	2.18	none	none	none	complete overcast
27 Jul	early	none	0.02	0.25	1.68	none	0.34	1.46	cloudy
6 Aug	peak	none	0.12	0.28	1.55	none	0.38	0.65	complete overcast
23, 26 Aug	peak	trace (0.005 m)	0.08	0.43	>2.5	0.07	0.33	0.85	complete overcast
3 Sep	freeze-up	0.02	0.08	0.26	1.43	0.12	0.36	0.59	complete overcast

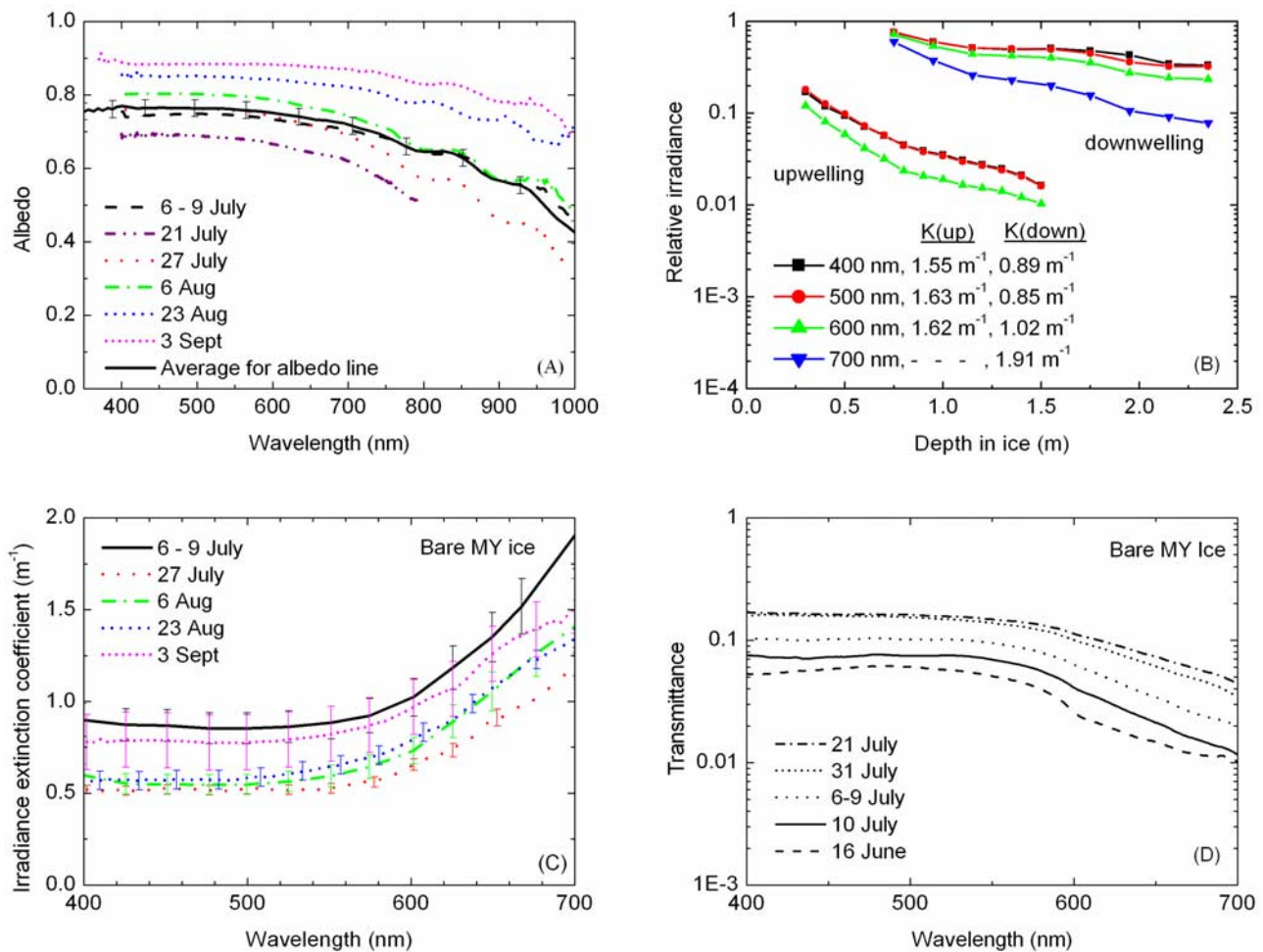


Figure 3. Optical properties of bare MY ice. (a) Spectral albedo, (b) vertical profiles of normalized up- and downwelling irradiance from 6 to 9 July, (c) spectral irradiance extinction coefficient, (d) spectral transmittance from five dates during melt season. Because ice thickness varies with location, the apparent increase in transmittance with time is not necessarily indicative of increasing ice transparency. As the 21 July albedo was measured with the ASD spectrophotometer, it was recorded for a reduced wavelength range. The 23 August and 3 September albedos are large due to the effects of trace amounts of snow at the surface. The 21 July albedo appears low likely because of reduced scattering at the immediate surface of the ice. Uncertainty indicated in Figure 3c shows larger values where ice interior light levels were lowest.

in Figure 3b for 6 July at four wavelengths. The legend also indicates K_λ values estimated from least squares regressions of the natural log of the irradiance profiles. These coefficients are reported for the four wavelengths shown for the upwelling and downwelling profiles, respectively. The downwelling irradiance extinction coefficients are reported for the 0.35–0.75 m depth interval. The upwelling irradiance extinction coefficients are reported for the depth interval 0.7–1.4 m and show significantly larger values. The distinction between upwelling and downwelling irradiance fields will be discussed later (see Figures 9 and 10).

[25] Values of K_λ calculated from equation (1) using the profiler data acquired for downwelling irradiance are shown in Figure 3c with error estimates derived from the root-mean-square deviation from fitting exponential curves to the profiles. The observed values of K_λ show a broad minimum near 500 nm generally corresponding to the maximum in α_λ with a strong increase in the near-infrared. The increases at shorter wavelengths depend on absorption by biological or inorganic material within the ice.

[26] Spectral transmittance measurements using the under ice arm recorded during June and July are shown in Figure 3d. Peak values in transmittance (approximately 0.17) occurred at wavelengths between 400 and 500 nm. Transmittance decreases at longer wavelengths as the absorption by ice and brine increases. The 21 July study site did not include profiler measurements, but the properties of the ice on that date were well characterized so it was chosen for further analysis. To give an idea of the variability of transmittance for bare MY ice, additional transmittance curves are shown for 16 June, 6–9 July, 10 July, and 31 July.

4.2. Ponded Multiyear Ice

[27] Figure 4a shows spectral albedos and Figure 4b shows K_λ values for ponded ice measured at the sites described above. Figure 4c shows spectral transmittance for selected ponded sites on 10, 21, and 31 July. The late summer pond measurement was made on 26 August, 3 d after the bare ice measurement. For ponded ice, the spectral albedos had a peak value of approximately 0.55 at about 500 nm. These albedos are considerably smaller than the bare ice values. The average albedo for ponded ice along the albedo line is shown, along with its standard deviation [Perovich *et al.*, 2002]. The irradiance extinction coefficients were typically, although not always, smaller than those for the bare ice cases. The greatest contrast, however, was in spectral transmittance, which was considerably larger for ponds, with the 21 July transmittance peak value of 0.4 in contrast to 0.17 for bare ice. Cases from 10 July and 31 July are also shown for the purpose of illustrating variability.

4.3. Bare and Melting First Year Ice

[28] The optical properties of first-year ice were investigated on two occasions, on 26 June during the early part of the melt season and on 15 August during the height of melt. Neither case included ponded ice. Physical properties and a description of the incident light conditions are given in Table 2 and optical measurements are shown in Figure 5. The albedo was similar to that for bare MY ice. Extinction coefficients were also similar to the values at the MY ice sites described previously. The transmittance measured on 26 June shows a strong chlorophyll absorption signature,

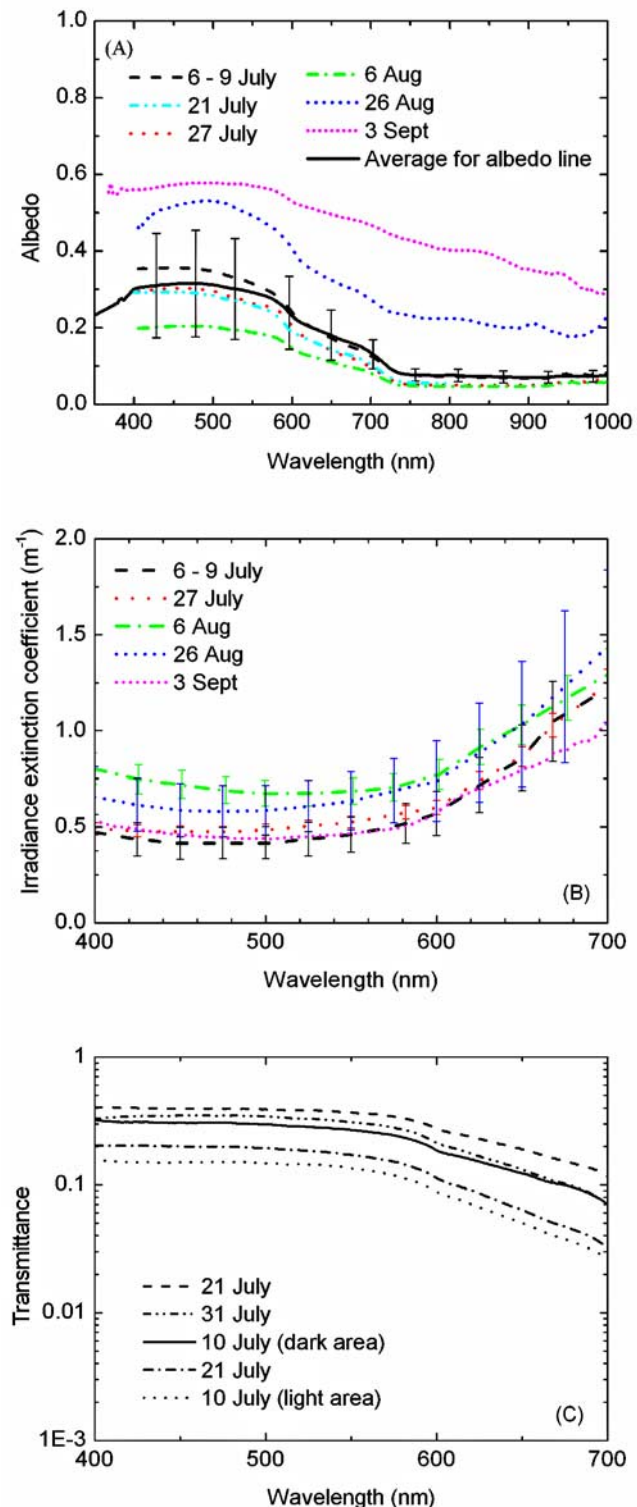


Figure 4. Optical properties of ponded MY ice. (a) Spectral albedo, (b) spectral irradiance extinction coefficient, and (c) spectral transmittance. Note that the ponds on 26 August and 3 September had formed thin ice skins which collected some of the new snow.

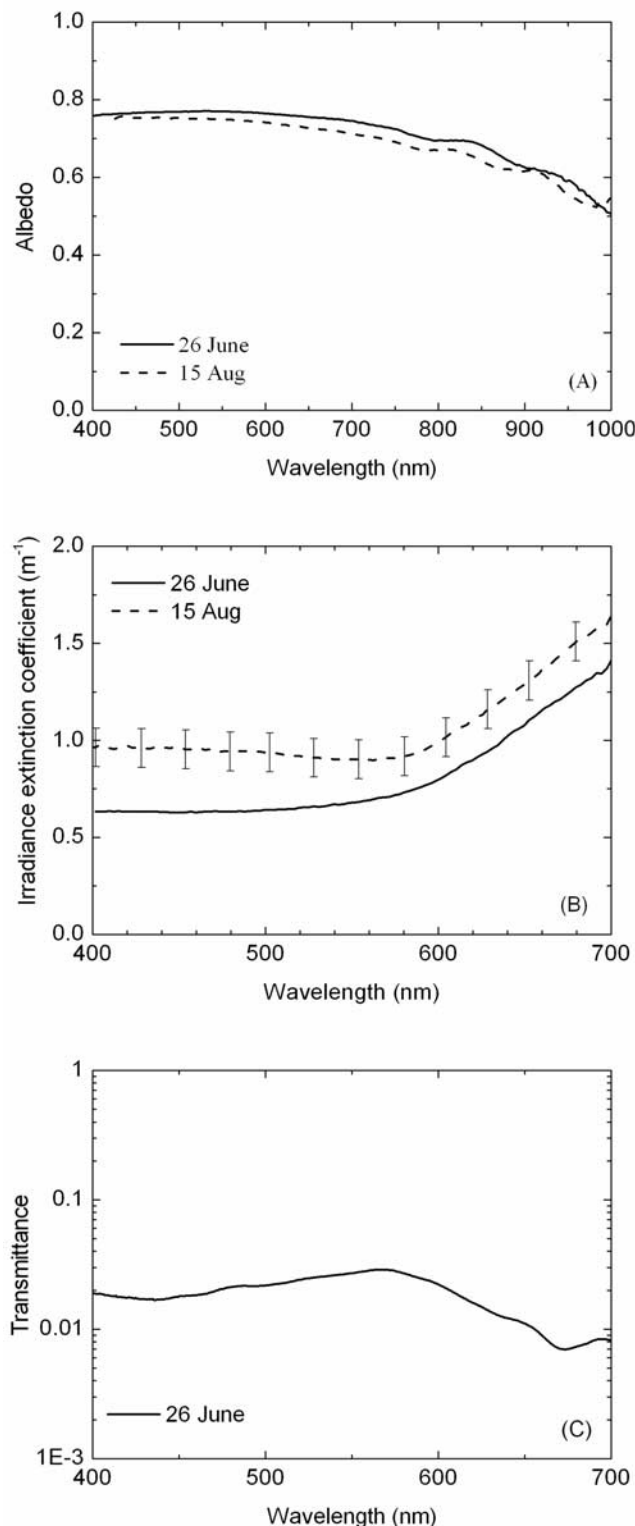


Figure 5. Optical properties of bare FY Ice. (a) spectral albedo, (b) spectral irradiance extinction coefficient, and (c) spectral transmittance. Note that the 26 June case had 0.05 m of snow at the surface, which has comparable effect on the albedo as the fully developed surface scattering layer of 15 August. The transmittance in Figure 5c shows indications of absorption by chlorophyll *a* within the ice, most specifically enhanced absorption at wavelengths shorter than 500 nm.

Table 2. Physical Properties and Incident Light Conditions for First-Year Ice and Multiyear Sediment-Laden Ice Cases^a

	First-Year Ice		Sediment-Laden Ice
	26 Jun	15 Aug	14 Jul
Snow cover (m)	0.05	none	none
Surface scattering layer thickness (m)	NA	0.04	0.18–0.20 (SSL + DL)
Freeboard (m)	0.18	0.09	0.40 (clean)/0.19 (with SPM)
Ice thickness (m)	1.53	1.0	2.50 (clean)/1.90 (with SPM)
Incident light conditions	highly variable	complete overcast	complete overcast

^aAbbreviations “SSL” and “DL” refer to “surface scattering layer” and “drained layer,” respectively. “SPM” is “suspended particulate material”.

excess absorption between 400 and 500 nm with a pronounced minimum near 420 nm and a notch at about 680 nm. This is consistent with clean interior ice with a layer of biological material on the bottom [Maykut and Grenfell, 1975; Perovich *et al.*, 1993].

[29] The 15 August site had 1 m thick ice with a 0.04 m thick SSL. The floe was undeformed, flat, and melt ponds were scarce. Extinction coefficients for this site are relatively large and show a chlorophyll absorption signature for the interior of the ice. Spectral transmittance was not measured at this site.

4.4. Sediment-Laden Multiyear Ice 14 July

[30] Several floes in the vicinity of SHEBA had suspended particulate material (SPM) within the ice. A study site was chosen in an area containing such visible sediment inclusions. Measurements were made in a dirty area as well as an adjacent area that appeared clean to the eye. The thicknesses were 2.50 and 1.90 m for the clean and SPM-laden ice, respectively. Physical properties are given in Table 2 and observed AOPs are shown in Figure 6. The resulting irradiance extinction coefficients are very distinct. K_λ for the clean ice is quite similar to the cases shown above, but the values for SPM laden ice are much larger (about 1 m^{-1} higher at 500 nm) and show an increase at shorter wavelength consistent with the brown color of the entrained material. The spectral transmittance is reported for the sediment laden ice and shows a magnitude comparable to the first-year ice with absorption by chlorophyll *a*. The transmittance is a factor of 2 or more smaller than the transmittance for bare multiyear ice measured on 21 July (Figure 3) with comparable ice thickness.

5. Time Series of K_{600}

[31] Although a detailed time series from this data set is complicated by the selection of different sites to avoid the disturbance caused by drainage through existing boreholes in the ice, a useful indication of the evolution of the irradiance extinction coefficient is presented in Figure 7. This shows the variation of K_{600} for the different sites spanning the observational period. Use of wavelength 600 nm is optimal in that it minimizes the influence of absorption by biogenic and terrigenous inclusions in the ice while retaining a useful level of transmitted radiation. All the irradiance extinction coefficients shown were calculated directly from profiler measurements, except

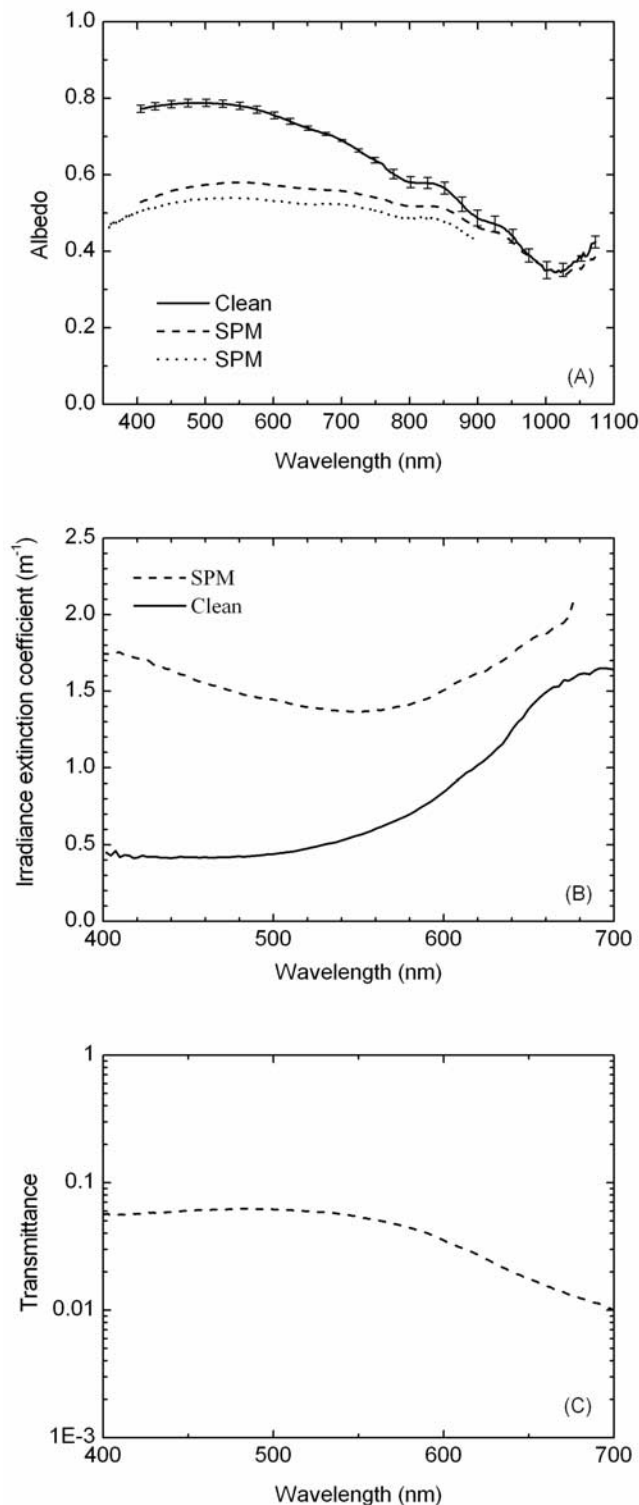


Figure 6. Observations of clean and sediment-laden (“SPM”) multiyear ice on 14 July. (a) Spectral albedo, (b) spectral irradiance extinction coefficient, and (c) spectral transmittance (for sediment laden ice).

the 21 July value, which was inferred from the spectral transmittance measurement using a radiative transfer model. Values of K_{600} shown are applicable to the interior of the ice.

[32] The median irradiance extinction at 600 nm for the bare ice cases is close to 0.8 m^{-1} with a corresponding value of about 0.6 m^{-1} for the melt ponds. For contrast we have also included results from early in the melt season shortly after the onset of pond formation (16 June). Representative values for K_λ are shown in Table 3 for wavelengths 500, 600, and 700 nm.

[33] Qualitatively, the data suggest three phases in the progression of summer melt. Initially (June–July), the irradiance extinction is higher for bare ice than it is for newly ponded ice. As melt progresses (August) the irradiance extinction within both bare and ponded ice is small and comparable. During the onset of freeze-up (early September), the bare ice irradiance extinction increases while the ponded ice irradiance extinction remains low.

[34] Several conditions associated with the progression of sea ice melt may help explain these observations: (1) once a shallow pond forms, the albedo of the ice drops precipitously, (2) ponded ice has a reservoir of liquid water at its surface, and (3) the propagation of surface cooling within the ice interior is delayed in ponded ice until the reservoir has frozen. The June and July data, where irradiance extinction coefficients are higher for bare ice than for ponded ice, suggest conditions 1 and 2. Ice that has formed a shallow surface puddle has a lower albedo and hence higher levels of shortwave radiation penetrate the ice surface. The absorption of this radiation causes brine inclusions within the ice to enlarge rapidly and to become interconnected. As brine inclusions interconnect, we expect gas inclusions to coalesce. Once pathways between the ice interior and surface are established, gas inclusions escape upward as bubbles, leaving behind voids that are subsequently filled with liquid water from the surface. The escape and subsequent flooding of gas voids would likely cause the scattering in interior ponded ice to be reduced. This process takes more time within bare ice. While there is no source of standing water at the surface, there is continual surface ablation and drainage of melt water into the interior. We suggest that this ushers in a second phase of melt, where the

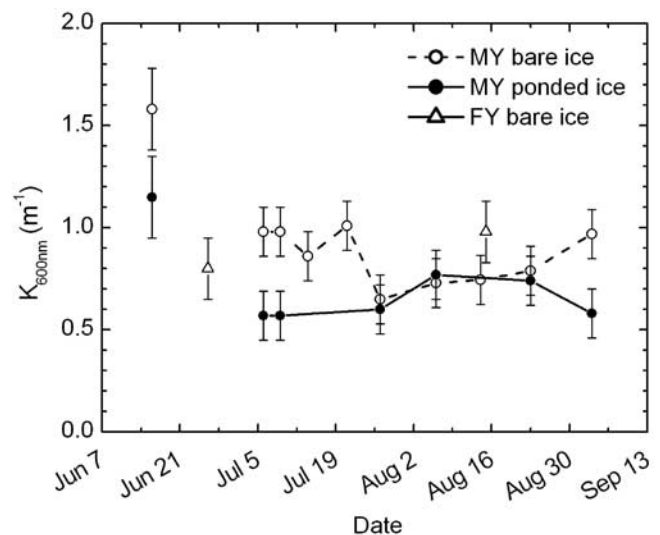


Figure 7. Downwelling irradiance extinction coefficient at 600 nm ($K_{600\text{nm}}$) for the various sites described as a function of date of observation.

Table 3. Downwelling Irradiance Extinction Coefficients (K_λ , in units of m^{-1}) for Each Site at Selected Wavelengths^a

Date	Bare Ice 500 nm	600 nm	700 nm	Melt Pond 500 nm	600 nm	700 nm	Comments
6–9 Jul	0.86	0.98	1.81	0.42	0.57	1.22	MY ice
27 Jul	0.52	0.65	1.20	0.49	0.60	1.24	MY ice
6 Aug	0.55	0.73	1.41	0.67	0.77	1.30	MY ice
23 Aug	0.58	0.79	1.34	0.59	0.74	1.44	MY ice
3 Sep	0.78	0.97	1.52	0.44	0.58	1.04	MY ice
14 Jul	0.44	0.86	1.63	-	-	-	clean MY ice adjacent, no pond
14 Jul	1.45	1.52	2.40	-	-	-	sediment-laden MY ice, no pond
26 Jun	0.64	0.79	1.42	-	-	-	FY ice, no pond
15 Aug	0.93	0.98	1.64	-	-	-	FY ice, no pond

^aIce type is specified to be multiyear (MY) or first-year (FY).

structure of the interior bare ice catches up to the ponded ice. We also suggest a final phase which is characterized by the onset of surface freezing. The interior of bare ice cools and refreezes, while the ice beneath ponds experiences delayed freezing. The rapid freezing in bare ice causes inclusions of brine to become isolated, thus producing more scattering. The interior of ponded ice remains unaffected by the transition to freezing conditions until the pond water freezes completely. Clearly, a more detailed data set is needed to validate this hypothesized sequence of conditions and their effects on the observed optical properties of the ice.

[35] Considering the ensemble of sites represented in Figure 7, however, it should be kept in mind that each data point represents ice at an individual location within the general area, and no one site was measured repeatedly. Thus some of the variability seen in Figure 7 likely represents site-to-site fluctuations superposed on a temporal evolution.

6. Comparison With Previous Results

[36] The irradiance extinction coefficients determined here are compared with the results of *Grenfell and Maykut* [1977, hereinafter referred to as GM77] measured on sea ice adjacent to ice island T-3 in the summer of 1974 at 84°N latitude. Figure 8 shows the current results plotted together with the GM77 curves for MY bare ice (Figure 8a), ponded ice (Figure 8b), and FY ice (Figure 8c). It is clear from Figure 8 that there is considerable variability in the irradiance extinction properties of bare and ponded ice. Extinction coefficients for the interior of bare multiyear ice are, in general, significantly lower than the GM77 values (approximately 0.5 to 0.85 m^{-1} lower at 600 nm). Several things may contribute to this difference. The GM77 results were obtained in a zone where the ice dynamics and deformation were considerably different. In addition, the earlier instrument was much less efficient and the data set much smaller. Finally, and probably most importantly, the irradiance extinction coefficients reported by GM77 for the interior ice were deduced from transmittance observations using a simplified radiative transfer model to remove the large effect of the scattering occurring in the near-surface layers of bare, melting ice.

[37] K_λ for the melt ponds also tends to be lower than the corresponding GM77 curves (median value of 0.6 m^{-1} for the current results versus 0.8 m^{-1} at 600 nm) but are much closer than for bare MY ice. The GM77 value falls within the variability observed in this data set, at least at visible wavelengths. The longer wavelength results in the GM77

dataset are likely affected by the significantly lower spectral resolution of the instrument used in that study. Additionally, differences could arise from the effects of finite horizontal extent of melt ponds and the influence of the surrounding

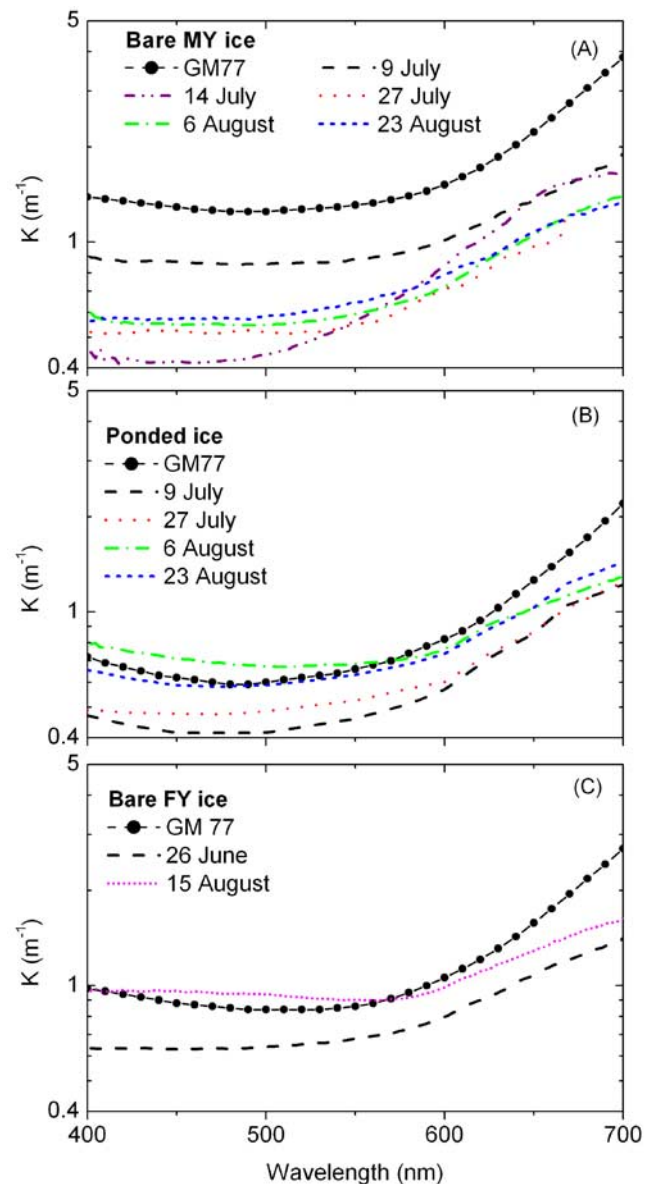


Figure 8. Comparison of the present values of K_λ with the results of *Grenfell and Maykut* [1977] for (a) bare MY ice, (b) ponded MY ice, and (c) bare FY ice.

bare ice. In general, the light field deeper in the ice has contributions from a larger areal extent at the surface. Thus irradiances deeper in the ponded ice may be influenced by the adjacent bare ice. The effect of such horizontal inhomogeneity would be to produce decreased irradiances at the lowest levels of the pond that underestimate the true irradiance, thus inflating the irradiance extinction coefficient calculated for ponded ice. GM77 did not report the precise size of the melt ponds so this error cannot be accurately evaluated. This error is a possibility in some parts of this data set as well. It is also possible that the irradiance extinction properties of the sea ice in 1974 are indeed different than found in this study. This could suggest there might be some sort of decadal variability in the optical properties of the ice cover, however, in view of the differences in location and melt intensity, as well as in instrumentation and procedures, this possibility remains difficult to evaluate.

[38] Owing to the improvements in virtually all aspects of the in-ice profiler and under-ice transmittance measurements as well as the more detailed sampling, we conclude that the irradiance extinction coefficients for the interior of bare multiyear ice should be revised downward. We expect this to have significant effect on climate models dealing with solar partitioning and the overall energy balance of the Arctic sea ice pack, as will be demonstrated in the following sections.

7. Optical Modeling

[39] There is a range of sophistication in how the partitioning of solar radiation is treated in sea ice models. In this section we present updated formulations for use in models of varying complexity for representing the penetration of shortwave radiation into sea ice and through to the ocean. The simplest schemes use the Bouguer-Lambert Law and K_λ , taking into account the nonexponential behavior in the surface layers by means of the partial transmission parameter I_0 , introduced by *Maykut and Untersteiner* [1971] and GM77 and presently used in the Community Climate System Model version 3 (CCSM3) [*Briegleb et al.*, 2004]. More sophisticated treatments explicitly calculate the effects of multiple scattering, requiring a vertical profile of inherent optical properties (IOPs) for the ice column [e.g., *Grenfell*, 1983, 1991; *Jin et al.*, 1994; *Briegleb and Light*, 2007]. We apply the radiative transfer models described in section 2 to interpret the optical observations and infer IOP values for the ice. In particular, we will assess the effect of borehole geometry on our results. We then derive models of the optical properties of the various types of ice studied. Specifically, we will use the present observations to determine vertical profiles of scattering coefficients. Such scattering coefficients are an inherent optical property and play a fundamental role in radiative transfer modeling. We will then use these inferred profiles to provide updated irradiance extinction coefficients for use in a GCM.

7.1. Simulations of the Detectors and the Borehole

[40] In addition to the local perturbation of the radiation field by the borehole, the probe used for measurement of downwelling radiation relied on a detector whose field of view excluded a cone from zenith to 15° , but the angular

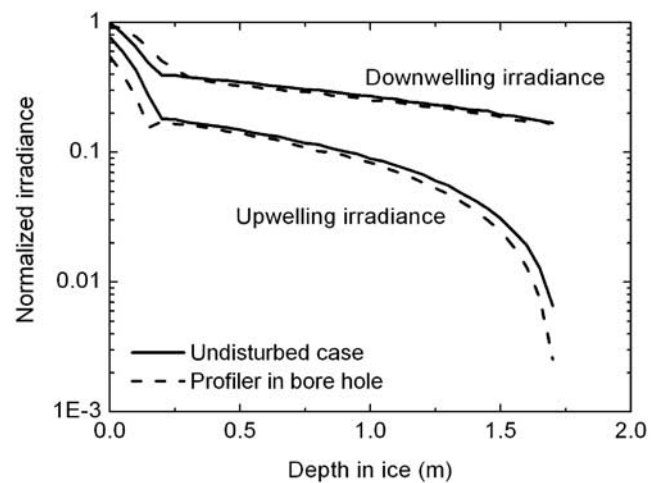


Figure 9. Irradiance profiles for upward and downward looking detectors in undisturbed ice (idealized case) and within a borehole simulated using the 2-D Monte Carlo radiative transfer model. The irradiances are normalized such that $F_{\text{down}}(0) = 1$. Irradiance extinction coefficients calculated for ice interior (0.4–0.7 m depth).

response from 15° to 90° closely matched that of an ideal cosine receptor. The influence of these effects compared to an ideal detector in an undisturbed medium was addressed using a 2-D Monte Carlo radiative transfer model (“2DMC”) [*Light et al.*, 2003a]. Figure 9 shows four model-predicted profiles for a two-layer representation (surface layer and interior layer) of the ice, in this case a 0.2 m thick highly scattering layer overlying 1.55 m of significantly reduced scattering interior ice. Representative IOPs were used (see next section) and the analysis was carried out for a wavelength of 500 nm, where the absorption by pure ice is small. The granular surface layer was assigned a bulk refractive index 1.0 and the interior layer 1.3. The borehole was filled with ocean water to the base of the surface layer at 0.2 m depth. This corresponds to 0.2 m of freeboard, which is about 0.05 m more freeboard than would be expected for this ice thickness. Of course the actual freeboard in nature would depend on the density profiles and ice thicknesses across an entire floe, not just on the ice at a single location. We chose to put the water level at 0.2 m depth for simplicity in the model. The detection of downwelling radiation was simulated using a cosine collector with the central 15° half angle cone masked. The detection of upwelling radiation was simulated with a cosine collector that sampled the full downward looking hemisphere, as was deployed in the field.

[41] Irradiance extinction coefficients for the four cases tested were computed from least squares regressions of the natural log of the irradiance profiles. The irradiance extinction coefficient calculated for downwelling irradiance in the ice interior (0.4–0.7 m depth) is 0.49 m^{-1} compared to 0.83 m^{-1} for the upwelling irradiance. This depth interval was chosen to be representative of the interval for which the observations were used to compute the K_λ values shown in Figures 3–8. Irradiance extinction coefficients calculated from upwelling radiation fields using equation (1) are generally larger than their downwelling counterparts. The

difference increases with depth and is due to the decay of the upwelling irradiance to zero at the ice-water interface, since the underlying ocean is assumed to scatter no light back into the ice. The near zero values of upwelling irradiance near the ice-ocean boundary cause upwelling K_λ values to be enhanced. This effect is clearly seen in the model results and is applicable to observed extinction coefficients as well [see also Grenfell, 1979]. Clearly, the upwelling irradiance at the ice-ocean boundary in nature will not be exactly zero, as in the model, but is generally small, as can be estimated from knowledge of the albedo of leads in the area, which was 0.066 [Pegau and Paulson, 2001].

[42] Although there is a clear difference between the slopes of the upwelling and downwelling profiles, the effects of the borehole and the limited field of view for the downwelling detector appear to be small, particularly in the interior of the ice. The model estimates interior irradiance extinction coefficients of 0.52 m^{-1} for the profiler in the borehole compared to 0.49 m^{-1} for the idealized undisturbed case. Because these deviations do not appear to cause significant or systematic differences in K_λ , we assume they are negligible (see Figure 9).

7.2. Ice Optical Properties

[43] On the basis of the prevalence of the observed ice structure as described in Figure 2j, we represent the vertical structure of bare, melting sea ice by a three layer model. This model consists of a surface scattering layer (SSL), a drained layer (DL), and interior ice, each of which has thickness denoted by z_i and distinct scattering coefficient ($\sigma(z_i)$). This structure was also motivated by the layer structure used for sea ice in CCSM3 [Briegleb et al., 2004]. At the surface, the absorption of a significant fraction of the incident solar radiation, including almost all of the infrared component, promotes considerable melt and metamorphism, leaving an intricate skeletal structure of fragile ice crystals permeated by void spaces. As a result, this surface layer exhibits the largest value of σ typically seen in the ice column. The drained layer roughly corresponds to the remainder of ice sitting above freeboard. Considerable scattering is observed in this layer as well, as the ice is also porous and drained. We call all the ice beneath the drained layer “interior ice.” While the largest scattering in the entire ice column is typically in the SSL, scattering in the drained layer is generally intermediate between the SSL and the interior ice. This three-step profile shows significant decreases in σ at both the SSL-DL and DL-interior boundaries.

[44] Pondered ice, on the other hand, generally shows a much more homogeneous structure throughout its depth. Although the ice-water interface in the ponds can be quite irregular, there are fewer isolated inclusions and fewer air-ice interfaces to scatter radiation, and the SSL is typically either absent or flooded. In some cases, embedded bubbles from previous overthrusting or deformation events can produce an internal scattering layer and a resulting increase in the albedo. This is often apparent during the early stages of melt. Higher melt pond albedos are often observed among ridged ice, due to the generally higher levels of volume scattering in the deformed ice beneath the puddled water.

[45] For each observation site, a three-layer (bare ice) or one-layer (pondered ice) vertical profile of scattering coefficients in the ice column was inferred from the observations

and a radiative transfer model. Initially, the analysis was carried out by using the observed spectral albedo (α_λ) to estimate the volume scattering coefficient as a function of depth using a layer stripping method. This method exploits the strong increase in absorption of both ice and water with wavelength by using the longest wavelength light back-scattered to infer information about the scattering properties of the top part of the ice. Less absorptive wavelengths are then examined to infer scattering information from layers residing successively deeper within the ice. This method takes advantage of the high accuracy and noninvasive nature of the spectral albedo observations to infer information about the IOPs in the surface and drained layers where direct measurements with the profiler are less accurate. In general, α_λ has a well-established spectral dependence and relative magnitudes show a maximum near 500 nm and a decrease in the infrared due to the increasing absorption of ice and water. The decrease at shorter wavelengths and the location of the maximum depend on the optical properties of the pure ice and brine as well as the optical properties of absorbing impurities within the ice. Both dissolved and particulate biogenic or terrigenous material can affect the albedo. Pond albedos are lower than that of bare ice because standing water fills voids in the surface layers, significantly reducing the volume scattering.

[46] To carry out the layer stripping procedure, a geometry using three layers of fixed geometric thickness was applied to the data from each of the study sites. For bare ice of thickness H , the lowest $0.75H$ comprised the interior ice. The uppermost 0.05 m thick layer was assigned to the SSL. Drained ice occupied the remaining ice between, its thickness being $(0.25H - 0.05) \text{ m}$. Freeboard at the various study sites was typically found to be somewhere within the drained layer. While it is possible that the layer stripping analysis would have been more accurate had individual drained layer thicknesses been adjusted to correspond directly with freeboard, assigning drained layer thickness to a fixed fraction of total thickness simplified and generalized the analysis. Furthermore, there is some suggestion that ocean water was frequently wicked into porous ice above freeboard (reducing the in situ scattering) and that ice just below freeboard may have higher scattering than interior ice, thus making it difficult to formulate a model whose drained layer depth is always constrained to be at the local freeboard. Pondered ice was assumed to have vertically uniform IOPs throughout its depth. Using this structure, the radiative transfer model was run iteratively for $\sigma(z_i)$ profiles that were within the range of expected values predicted by a structural-optical model [Light et al., 2004]. Each profile was then adjusted to converge on the best representation of the observed spectral albedo. Absorption coefficients were assigned based on fixed ice density profiles (420 , 830 , and 920 kg m^{-3} for the SSL, drained layer, and interior ice, respectively; 920 kg m^{-3} for all pondered ice). We assumed that the ice component contained only pure ice free of absorbing impurities [see Grenfell, 1991]. Because of its low density, the bulk refractive index of the SSL is set to 1.0 , analogous to the treatment of a snow layer in radiative transfer calculations. All remaining layers have refractive index of pure ice (~ 1.3). Scattering coefficients were assumed to be independent of wavelength, a good approximation for the expected size distribution of scatterers in sea

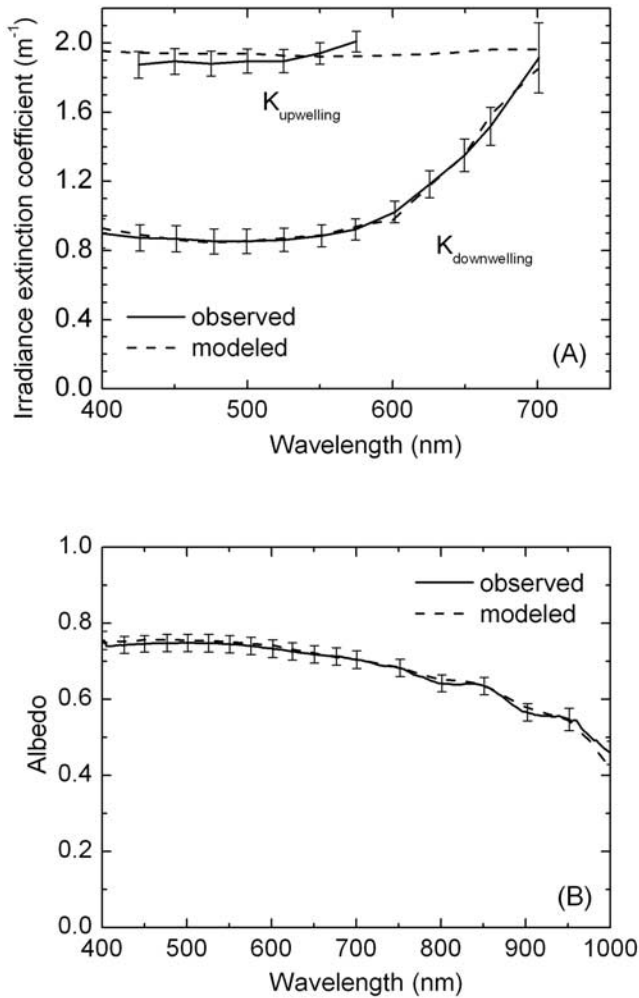


Figure 10. Observed and modeled (a) spectral downwelling and upwelling irradiance extinction coefficients and (b) spectral albedo for bare ice for 6–9 July. Error bars are standard deviations from seasonal ensembles.

ice [Light *et al.*, 2003b]. The asymmetry parameter, g , was assumed to be 0.94 at all wavelengths for computational efficiency. The asymmetry parameter is the cosine weighted average of the phase function, and varies from -1 (complete backscattering) to +1 (complete forward scattering). When the probability of being scattered in either the backward or forward hemisphere is equal, such as for isotropic scattering, g has value 0. While 0.94 is probably too low for the majority of actual g values appropriate for sea ice, a similarity principle given by van de Hulst [1980] and employed by Light *et al.* [2004] provides a relationship between g , $\sigma(z_i)$ and the absorption coefficient (κ),

$$\left[1 + \frac{\sigma}{\kappa}(1 - g)\right]^{-1/2} = \text{const.} \quad (2)$$

When comparing multiple (σ, g) pairs for a constant value of κ , equation (2) can be reduced to $\sigma(z) \cdot (1 - g) = \text{const.}$, which can be used to identify scaled σ values for different

values of g . As a result, all $\sigma(z_i)$ profiles were inferred assuming $g = 0.94$. This alleviated numerical instability associated with g values very close to unity in the radiative transfer model and provides for the comparison of $\sigma(z_i)$ profiles in different ice types, even if their values of g differ.

[47] Once an initial $\sigma(z_i)$ profile was established for the three-layer standard geometry, then the observed values of K_λ were used to refine $\sigma(z_i)$. Typically, this adjustment occurred in the ice interior, where uncertainties in the $\sigma(z_i)$ inferred strictly from the spectral albedo are largest. Figure 10 shows observed and modeled spectral albedos and irradiance extinction coefficients for the 6–9 July study site. The irradiance extinction of downwelling irradiance is taken for the depth interval 0.35–0.70 m and the irradiance extinction of upwelling irradiance is taken for the 0.70–1.10 m interval. As discussed above, the extinction coefficient for upwelling irradiance is considerably larger than the extinction coefficient for downwelling irradiance, as seen in both the observations and model. The modeled upwelling extinction shows little spectral variation. This can be explained by noting that at red wavelengths (e.g., 700 nm), where the ice is strongly absorbing, the downwelling and upwelling extinction coefficients are almost equal. At strongly absorbing wavelengths, a cosine collector detects mostly photons that have traveled the shortest paths through the ice, thus escaping extinction by absorption. The shortest path to a downward looking detector is one where the photon travels straight to the depth of the detector and is then backscattered into the detector. Of course, photons of many different histories will be collected at the detector, but the collection is biased to photons that have the shortest paths possible. These photons then suffer the same extinction as a downwelling photon captured by the upward looking detector, plus a little bit more as they are backscattered into the downward looking detector. Hence, the upwelling and downwelling extinction coefficients at the longer wavelengths are similar. At shorter wavelengths, where the absorption by ice is considerably smaller, photon paths through the ice to the detector can be considerably less direct, and the effect of the ice-ocean interface is felt. The majority of photons affected by this non reflecting interface and which would have survived far enough to contribute to a signal at a downward looking detector placed above the interface are those with wavelengths where absorption is smallest. The effect of the nonreflecting interface, as discussed earlier, is to increase the value of K for upwelling light. These effects are rigorously taken into account by the radiative transfer model, and the observations and the model show outstanding agreement. However, the upwelling extinction data only extend to 550 nm, so it is not possible to say whether the observations also show the spectrally neutral behavior seen in the model.

[48] When the analysis is constrained to this structure of fixed geometric depths and scattering coefficients that do not vary with wavelength, strong gradients in $\sigma(z_i)$ exist near the surface, where σ ranges from 500 m^{-1} to as high as 1100 m^{-1} in the SSL and decreases by a factor of 2 to 14 in the drained layer. Values for the surface layer on 23 August and 3 September include the effects of trace amounts of snow on the surface. Values of σ predicted for the interior of bare ice vary between 8 and 30 m^{-1} as shown in Figure 11a. Corresponding results for melt ponds are given in Figure 11b

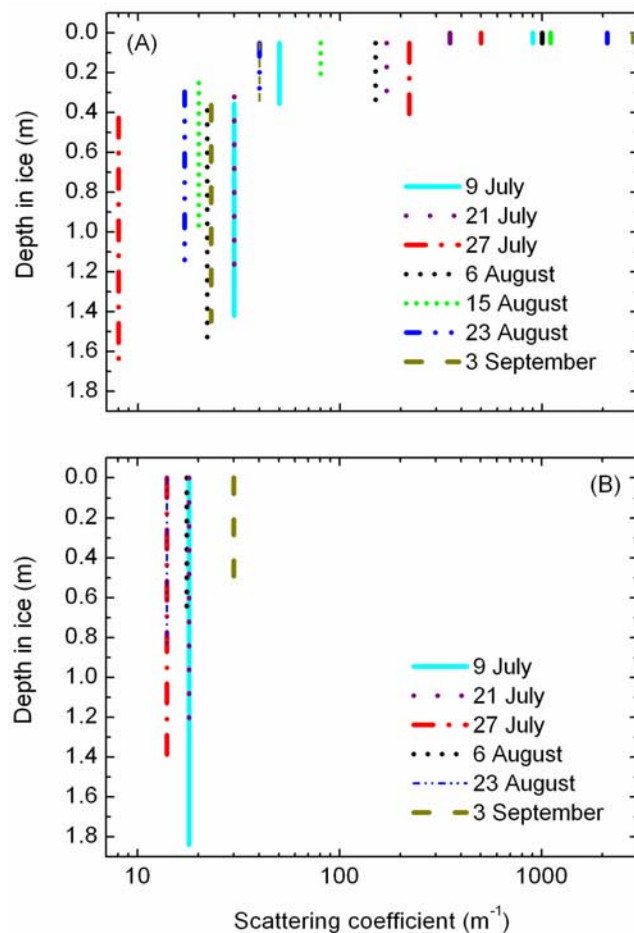


Figure 11. Vertical distribution of inferred scattering coefficients for (a) bare and (b) ponded ice observed in this study. Values of scattering coefficient were inferred from radiative transfer model calculations carried out to simulate observed irradiance extinction coefficients.

where the analysis is constrained to produce uniform values of σ independent of depth. The resulting values of σ for ponded ice vary from 15 to 30 m^{-1} .

[49] The estimated $\sigma(z_i)$ profiles produced by this approach are not necessarily unique. They merely reflect the profile best able to explain the observed spectral albedo, transmittance, and irradiance extinction given the imposed layer geometry. By setting distinct layers with fixed thicknesses, variations in $\sigma(z_i)$ actually correspond to variations in optical depth. The imposed layer structure is a simplification of the actual vertical structure of the ice, although the SSL and DL do tend to exist over finite depths and display obvious boundaries, at least when viewed after removal from the ice. Despite these oversimplifications, we feel this structure provides new insight relevant to modeling the partitioning of shortwave radiation by sea ice.

[50] Time dependent changes in the inferred scattering coefficients for the three layers of bare ice and single layer of ponded ice are shown in Figure 12. Scattering in the SSL shows an initial decrease with time, followed by a steady increase. Scattering in this layer also responds to transient

day-to-day fluctuations in surface conditions. For example, after sunny days a deepening of the layer was often observed, and after foggy conditions, the layer thickness was observed to decrease. Sunny conditions caused heating and melting within the layer as the direct sunlight penetrated through the uppermost surface of the ice. Foggy conditions caused moisture condensation at the surface, likely heating and melting the top part of the layer. Once the SSL was firmly established, its general trend was to show increased scattering with time as the sunlight continued to degrade the top surface of the ice. Since the modeled layer thickness was fixed at 0.05 m, the observed increase in scattering in the field represents either an increased scattering in a fixed depth layer, increased physical depth of the SSL, or a combination of the two. Because the SSL was observed to both deepen and exhibit textural changes in response to synoptic-scale variations in conditions, the combination appears to be most likely. As indicated in Figure 11, the SSL scattering for 23 August and 3 September includes the effects of a dusting of snow, so these values are likely enhanced beyond the value representative for the actual scattering within the ice.

[51] Figure 12 indicates that scattering in the drained layer showed an increase during the initial phase of melt and then proceeded to decrease steadily as melt progressed. Since the thickness of the layer is constrained in the model, the decreased scattering coefficient implies decreased optical depth, regardless of whether it is accomplished by decreasing the geometric thickness or decreasing the scattering coefficient. One possible scenario is that as the ice melts, bubbles in the drained layer enlarge and begin to coalesce. As this above-freeboard layer becomes more porous, melt water from above drains into the layer, filling the voids in the ice with water and further reducing the optical depth.

[52] The scattering coefficient within the ice interior is small and relatively constant with time. In ponded ice, σ does not appear to be distinct from the value found for the interior of bare ice. As a result, differences in transmission to the ocean derive from the presence/absence of a SSL and drained layer in addition to differences in total ice thickness.

[53] *Perovich et al.* [2002] observed that the albedo for bare, melting ice was approximately 0.65 ± 0.02 over the course of the melt season. At least some of the variability in bare ice albedo was due to changes in the thickness of the SSL. Increases in the scattering within the SSL alone would suggest that the albedo should also increase during the latter part of the melt season. Our results however, suggest that this increase in the scattering is offset by decreased scattering in the drained layer below. The net result is an approximately constant albedo.

7.3. Parameterization of AOPs

[54] We will now present a summary of the parameters derived from the AOPs found in this study that can be applied directly for use in GCMs. Existing parameterizations commonly used by such models rely on knowledge of the albedo, extinction coefficient, and a surface transmission parameter, I_o for describing the interaction between the ice and incident shortwave radiation. I_o was designed to be a quantitative measure of the fraction of radiation transmitted through the highly scattering surface of the ice. Its use permits the

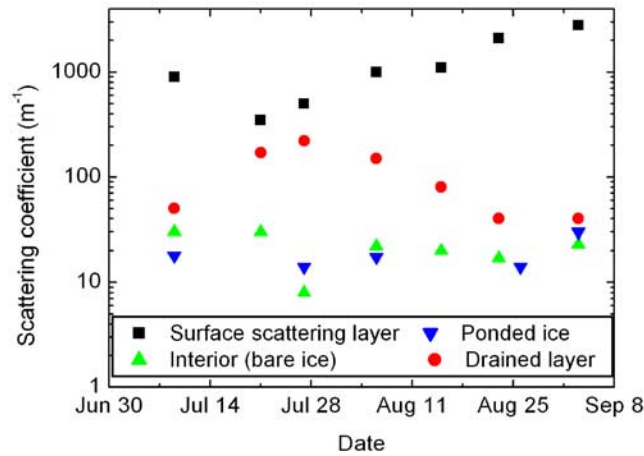


Figure 12. Time series of inferred scattering coefficients for bare and ponded cases in this study. Note that the 15 August first-year ice case is included in this time series.

calculation of shortwave downwelling flux at level z within or beneath the ice ($F_{sw}(z)$) to be given by equation (3):

$$F_{sw}(z) = F_{sw}(inc)(1 - \alpha)I_o \exp(-Kz), \quad (3)$$

where $F_{sw}(inc)$ represents the incident downwelling irradiance and α the albedo. Formulae for I_o and the wavelength-integrated K are given by equations (4) and (5), respectively.

$$I_o = \int_{\lambda_1}^{\lambda_2} F_{net,\lambda}(0.1m) \cdot d\lambda / \int_{\lambda_1}^{\lambda_2} F_{net,\lambda}(inc) \cdot d\lambda \quad (4)$$

$$K = \int_{\lambda_1}^{\lambda_2} K_\lambda \cdot F_{net,\lambda}(0.1m) \cdot d\lambda / \int_{\lambda_1}^{\lambda_2} F_{net,\lambda}(0.1m) \cdot d\lambda. \quad (5)$$

Here, $F_{net,\lambda}(0.1m)$ is the spectral net flux at 0.1 m depth, $F_{net,\lambda}(inc)$ is the spectral net flux at the surface, and λ_1 and λ_2 indicate the wavelength range over which the integration takes place. The 0.1 m depth was established by Maykut and Untersteiner [1971] to conform to their usual grid spacing of 0.1 m.

[55] Table 4 shows values of albedo, I_o , and K for the near UV and visible ($350 \text{ nm} < \lambda < 700 \text{ nm}$) and near infrared ($700 \text{ nm} < \lambda < 3000 \text{ nm}$). Albedos for bare and ponded multiyear ice are average values taken from the albedo line at SHEBA [Perovich *et al.*, 2002]. The I_o values are specified for 0.1 m depth, so that they may be most applicable to existing models.

[56] $K(vis)$ values are averages of observed values and $K(nir)$ values were calculated using a one-dimensional four-stream discrete ordinates radiative transfer model (1DRTM) [Grenfell, 1991] and the IOPs presented above adjusted to produce a consistent extrapolation of the spectral irradiance extinction coefficient into the infrared. This was necessary because the light levels were too low for reliable direct

estimates of irradiance extinction coefficients measured at these wavelengths. The first-year ice K value is the average of 26 June and 15 August, and it includes a substantial contribution from absorption by biogenic inclusions.

8. Radiative Partitioning

[57] Presumably, knowledge of the albedo at a particular location and time specifies the portion of incident radiation absorbed within the ice-ocean column. Radiation not back-scattered to the atmosphere must be absorbed somewhere in the ice or the ocean. Radiation absorbed in the surface layers will contribute to surface ablation. Radiation absorbed in the interior of the ice will contribute to an increase in temperature and eventually interior melting in the form of an increase in brine volume or will be available for in-ice biologic processes. Radiation that penetrates through the ice will be absorbed in the ocean and available to biologic communities in the water column. This radiative energy absorbed in the ocean may be available to locally melt the ice through which it originally penetrated or it may be stored in the ocean mixed layer and advected laterally to become available to melt ice of a different type or thickness. Each of these mechanisms affects the mass balance of the ice in different ways and with varying time lags. For these reasons, it is important to develop a quantitative understanding of how the absorbed radiation is partitioned.

[58] GM77 suggested representative I_o values of 0.70 and 0.0 for the visible and near-infrared bands respectively. The present values shown in Table 4 indicate that I_o should be significantly larger for both bands (≥ 0.93 for the visible; ≥ 0.26 for the near-infrared). This increase gives way to the deeper penetration of substantially larger amounts of radiation within the ice.

[59] The $\sigma(z_i)$ profiles established for each study site were used to calculate the penetration of light to different depths within the ice/ocean column in the 1DRTM. For this analysis, we focus on the $\sigma(z_i)$ model inferred for 6 August. This date is felt to be representative of summer multiyear ice observed during this study. The $\sigma(z_i)$ model for 6 August was used to calculate the penetration of light in and through ice of various thicknesses. For comparison, we used the shortwave radiation partitioning parameterization of CCSM3 [Briegleb *et al.*, 2004] which is based on GM77, with $I_o(vis) = 0.7$, $I_o(nir) = 0.0$, and $K(vis) = 1.4 \text{ m}^{-1}$.

[60] Figure 13 shows vertical profiles of absorbed radiation for visible and near-infrared radiation calculated using the 1DRTM (6 August) compared with the calculation of CCSM3. Since we are not including an atmospheric component in either of these radiative transfer calculations, we arbitrarily assumed the incident downwelling irradiance at the ice surface to be 100 W m^{-2} for each of the two wavebands for all cases. Figures 13a and 13b show this comparison for 1 m thick ice.

[61] Because the parameterized albedo predicted by CCSM3 (0.72 for the visible, 0.38 for the near-infrared) is similar to the 1DRTM predicted albedo for 6 August (0.77 for the visible, 0.61 for the near infrared), at least at visible wavelengths, the total amount of shortwave radiation absorbed is comparable for the two calculations. However, the amount penetrating deep into the ice and transmitted to

Table 4. Albedo, I_o , and K for Different Ice Types^a

Ice Type	Alb(vis)	Alb(nir)	$I_o(vis)$	$I_o(nir)$	$K(vis) \text{ m}^{-1}$	$K(nir) \text{ m}^{-1}$
Melting MY ice	0.753 ± 0.023	0.454 ± 0.028	0.93	0.26	0.794	4.74
Melting FY ice	0.744	0.560	0.97	0.29	0.930	4.76
Ponded MY ice	0.251 ± 0.115	0.081 ± 0.022	0.99	0.48	0.645	4.38

^a I_o values are estimated from 1DRTM simulations for the visible (350–700 nm) and near infrared (700–3000 nm). $K(vis)$ values are based on observations, and $K(nir)$ values are determined from model results integrated between 700 and 1000 nm.

the ocean is significantly different for the two cases. The 1DRTM calculation shows 14.1 Wm^{-2} reaching the ocean at visible wavelengths and 1.1 Wm^{-2} at near infrared wavelengths. The CCSM3 calculation predicts a total of 4.9 Wm^{-2} reaching the ocean, all in the visible band. For this case, the parameters derived from this study predict a threefold increase in solar radiation reaching the ocean relative to the CCSM3 calculation. This difference between the existing model and the present analysis is driven by two factors: the larger penetration of energy through the surface and the decreased extinction of energy within the interior. As shown in Table 4, the new I_o value for melting MY ice is 0.93, indicating that only a fraction of 0.06 of the total energy in the visible waveband is absorbed in the surface layer. In CCSM3, the radiation is largely absorbed in the surface layers (I_o values of 0.70 in the visible and 1.0 in the near infrared cause fractional energy of 0.3 in the visible and 1.0 in the near infrared to be absorbed in the surface layer), whereas our analysis indicates it actually penetrates deeper into the ice and a considerable amount penetrates all the way through to the ocean.

[62] Thicker ice cases show similar behavior. Figures 13c and 13d show the absorbed irradiance (also assuming 100 Wm^{-2} incident for each band) calculated using this analysis and the CCSM3 parameterization for 3 m thick ice. Albedos are 0.81 and 0.61 for the visible and near infrared respectively for the 6 August case. For CCSM3 they are 0.73 and 0.38, respectively. In this case, our analysis yields an input of 3.2 Wm^{-2} to the ocean, compared to 0.3 Wm^{-2} in CCSM3. Both calculations show zero penetration in the near infrared. This comparison suggests that significant increases in total transmitted energy result from the decreased values of K_λ found in the present study, along with the significantly larger amount of radiation permitted to penetrate below the surface layer.

[63] We have also computed spectral transmittances for ponded ice. For a 0.4 m deep pond underlain by 1.0 m of ice, 47.3 Wm^{-2} penetrates to the ocean at visible wavelengths and 3.2 Wm^{-2} penetrates in the near infrared. Again, 100 Wm^{-2} was incident at the surface in each band. This is approximately three times more radiation penetrating to the ocean than the 1 m thick bare ice case. Likewise, for 3.0 m thick ponded ice (0.4 m pond depth), 15.1 Wm^{-2} and 0.1 Wm^{-2} are predicted to penetrate to the ocean in the two bands respectively. Since CCSM3 has no explicit ice type designated for ponded ice, we cannot make a relevant comparison. Furthermore, the CCSM3 estimates for melting bare ice implicitly include the effects of ponded ice, through a lower albedo, and thus should be biased towards penetrating additional radiation deeper into the ice relative to the bare, melting white ice case used in the 1DRTM calculation. Yet, the comparisons show just the opposite. This analysis

suggests that more of the incident radiation is penetrating the ice and being absorbed in the ocean than has been previously identified. Since the CCSM3 parameterization uses the irradiance extinction coefficient established by GM77 as its basis for computing the penetration of radiation, any model using the GM77 results will likely be predicting higher attenuation in the ice, particularly at the surface, than the current results establish.

9. Conclusions

[64] Experiments carried out during the SHEBA field investigation focused on determining the optical properties of melting MY ice and using them to assess the partitioning of solar radiation by bare and ponded sea ice during the summer melt season. Sites chosen for the optical and physical characterization of the ice included bare and ponded multiyear ice, first-year ice, and sediment laden multiyear ice. Measurements of the spectral albedo, spectral irradiance profiles of upwelling and downwelling irradiance through the ice column, and spectral transmittance were made at these sites.

[65] Extinction coefficients were calculated directly from profiles of downwelling irradiance. For bare, melting multiyear ice, the representative integrated irradiance extinction coefficients are smaller than those previously established [Grenfell and Maykut, 1977] by approximately a factor of 2. The present analysis results in irradiance extinction coefficients for the interior of melting ice that range from 0.65 to 0.98 m^{-1} at 600 nm. These values are considerably smaller than the previously accepted value of 1.5 m^{-1} . The effect of this is that more light is predicted to penetrate deep into the ice and into the ocean than was previously accounted for. It has been established that ponded ice transmits a significant amount of shortwave radiation to the ocean [Perovich, 2005] relative to the oceanic heat flux at the bottom of the ice. In fact, ponded ice (of comparable thickness) likely transmits 3–5 times more solar radiation to the ocean. But the present study suggests that the transmittance through bare, melting ice is also significant, and our calculations suggest that as much as 3% of the incident radiation may penetrate 3 m thick ice while 15% may penetrate 1 m thick ice.

[66] This analysis also demonstrates that there exist distinct layers with large vertical differences in scattering coefficient within bare ice, while ponded ice can generally be simulated using a vertically homogeneous scattering profile. Bare, melting ice requires at least a three-layer representation, and scattering coefficients near its surface were found to be $500\text{--}1100 \text{ m}^{-1}$ (for asymmetry parameter $g = 0.94$). Scattering coefficients for interior ice and ponded ice were found to be 1–2 orders of magnitude smaller ($8\text{--}30 \text{ m}^{-1}$). This pattern results from the presence of a highly

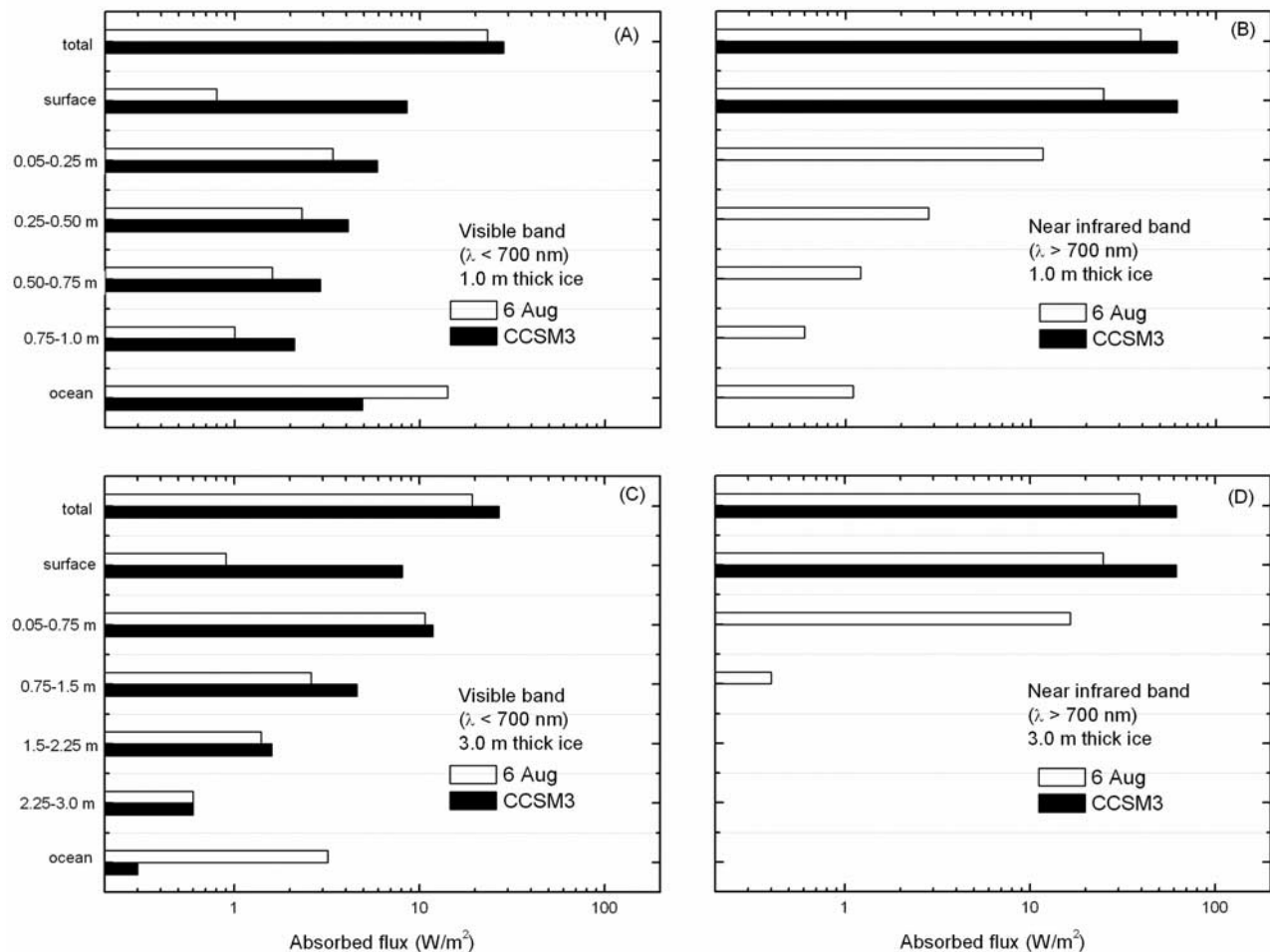


Figure 13. Model predictions of absorbed shortwave energy flux in 1.0 m and 3.0 m thick bare, melting ice. (a and b) Visible and near infrared radiation bands for the 1.0 m thick case, and (c and d) the visible and near infrared radiation bands for the 3.0 m thick case. The vertical axis shows the depth in the ice. For each band, incident downwelling irradiance of 100 W m^{-2} was assumed at the surface. Surface albedos are 0.77 and 0.61 for visible and near infrared bands for the 6 August simulation of 1 m thick ice. They are 0.72 and 0.38 for the corresponding bands in the CCSM3 calculation. Surface albedos are 0.81 and 0.61 for visible and near infrared bands for the 6 August simulation of 3 m thick ice. They are 0.73 and 0.38 for the corresponding bands in the CCSM3 calculation.

scattering surface layer that develops at the beginning of the melt season and is sustained as the ice surface ablates. As a result of this layer, the penetration of light within the ice and the transmission of light to the ocean are controlled partially by the irradiance extinction of interior ice but also by the strong backscattering at the surface. This surface layer contributes substantially to the relatively large albedo (approximately 0.65) of melting bare ice and thus is critical to the interaction of solar radiation with the summer sea ice cover. For the most part, ponded ice lacks a significantly long lasting surface scattering layer and is thus a strong transmitter of solar radiation to the ocean.

[67] While the albedo of bare, melting ice has been observed to remain approximately constant over the course of a melt season [Perovich *et al.*, 2002], our analysis suggests that scattering in the individual layers evolves during the melt season; however, increases in scattering in

the surface layer are approximately offset by decreases in the drained layer below, consistent with the notion of a stable albedo. In contrast, scattering within the interior of the ice is significantly smaller and tends to remain approximately constant. The presence of a surface scattering layer and drained layer are critical to the partitioning of shortwave radiation in the ice-ocean system.

[68] A model of the vertical structure of the scattering coefficient of the ice derived directly from our field observations was developed such that the partitioning of radiation by specific types of sea ice could be studied. The analysis found that the model predicts 3–10 times more solar radiation penetrating the ice cover than a current GCM parameterization (CCSM3). The exact ratio depends on ice thickness, stage of the melt season, and particular scattering profile. This current GCM parameterization is based on the irradiance extinction coefficient presented by Grenfell and

Maykut [1977] which we believe significantly underestimates the amount of sunlight reaching the ocean for a typical summer ice cover. The present study indicates that transmitted radiation through summer ice needs to be taken into account to properly understand regional shortwave energy partitioning and resulting ice-radiation feedback processes.

[69] **Acknowledgments.** We gratefully acknowledge support from the National Science Foundation (ARC-0531018), the Office of Naval Research (N00014-97-1-0765 and N00014-03-1-0120), and NASA (NNG06HMI8I and NNNH04AA71I-1). We also thank B. Briegleb for fruitful discussion and helpful comments on this manuscript.

References

- Bitz, C. M., M. M. Holland, A. J. Weaver, and M. Eby (2001), Simulating the ice thickness distribution in a climate model, *J. Geophys. Res.*, **106**, 2441–2463.
- Briegleb, B. P., and B. Light (2007), A Delta-Eddington multiple scattering parameterization for solar radiation in the sea ice component of the Community Climate System Model, *NCAR/TN-472+STR*, 100 pp., Natl. Cent. for Atmos. Res., Boulder, Colo.
- Briegleb, B. P., C. M. Bitz, E. C. Hunke, W. H. Lipscomb, M. M. Holland, J. L. Schramm, and R. E. Moritz (2004), Scientific description of the sea ice component in the Community Climate System Model, version 3, *NCAR/TN-463+STR*, 70pp., Natl. Cent. for Atmos. Res., Boulder, Colo.
- Cavalieri, D. J., C. L. Parkinson, and K. Y. Vinnikov (2003), 30-Year satellite record reveals contrasting Arctic and Antarctic decadal sea ice variability, *Geophys. Res. Lett.*, **30**(18), 1970, doi:10.1029/2003GL018031.
- Clarke, A. D., and K. J. Noone (1985), Soot in the Arctic snowpack - A cause for perturbations in radiative-transfer, *Atmos. Env.*, **19**, 2045–2053.
- Comiso, J. C., J. Y. Yang, S. Honjo, and R. A. Krishfield (2003), Detection of change in the Arctic using satellite and in situ data, *J. Geophys. Res.*, **108**(C12), 3384, doi:10.1029/2002JC001347.
- Curry, J. A., J. L. Schramm, and E. E. Ebert (1995), Sea-ice albedo climate feedback mechanism, *J. Clim.*, **8**, 240–247.
- Ebert, E. E., and J. A. Curry (1993), An intermediate one-dimensional thermodynamic sea-ice model for investigating ice-atmosphere interactions, *J. Geophys. Res.*, **98**, 10,085–10,109.
- Ebert, E. E., J. L. Schramm, and J. A. Curry (1995), Disposition of solar-radiation in sea-ice and the upper ocean, *J. Geophys. Res.*, **100**, 15,965–15,975.
- Eicken, H., T. C. Grenfell, D. K. Perovich, J. A. Richter-Menge, and K. Frey (2004), Hydraulic controls of summer Arctic pack ice albedo, *J. Geophys. Res.*, **109**, C08007, doi:10.1029/2003JC001989.
- Grenfell, T. C. (1979), The effects of ice thickness on the exchange of solar radiation over the polar oceans, *J. Glaciol.*, **22**, 305–320.
- Grenfell, T. C. (1983), A theoretical model of the optical properties of sea ice in the visible and near-infrared, *J. Geophys. Res.*, **88**, 9723–9735.
- Grenfell, T. C. (1991), A radiative-transfer model for sea ice with vertical structure variations, *J. Geophys. Res.*, **96**, 16,991–17,001.
- Grenfell, T. C., and G. A. Maykut (1977), The optical properties of ice and snow in the Arctic basin, *J. Glaciol.*, **18**, 445–463.
- Grenfell, T. C., and D. K. Perovich (1984), Spectral albedos of sea ice and incident solar irradiance in the southern Beaufort Sea, *J. Geophys. Res.*, **89**, 3573–3580.
- Grenfell, T. C., and D. K. Perovich (2004), Seasonal and spatial evolution of albedo in a snow-ice-land-ocean environment, *J. Geophys. Res.*, **109**, C01001, doi:10.1029/2003JC001866.
- Grenfell, T. C., S. G. Warren, and P. C. Mullen (1994), Reflection of solar-radiation by the Antarctic snow surface at ultraviolet, visible, and near-infrared wavelengths, *J. Geophys. Res.*, **99**, 18,669–18,684.
- Grenfell, T. C., et al. (1998), Evolution of electromagnetic signatures of sea ice from initial formation to the establishment of thick first-year ice, *IEEE Trans. Geosci. Remote Sens.*, **36**, 1642–1654.
- Grenfell, T. C., B. Light, and M. Sturm (2002), Spatial distribution and radiative effects of soot in the snow and sea ice during the SHEBA experiment, *J. Geophys. Res.*, **107**(C10), 8032, doi:10.1029/2000JC000414.
- Grenfell, T. C., B. Light, and D. K. Perovich (2006), Spectral transmission and implications for the partitioning of shortwave radiation in arctic sea ice, *Ann. Glaciol.*, **44**, 1–6.
- Hanesiak, J. M., D. G. Barber, R. A. De Abreu, and J. J. Yackel (2001), Local and regional albedo observations of arctic first-year sea ice during melt ponding, *J. Geophys. Res.*, **106**, 1005–1016.
- Hayes, D. R. (2003), The heat and salt balances of the upper ocean beneath a spatially variable melting sea ice cover, *APL-UW TR 0302*, Appl. Phys. Lab., Seattle, Wash.
- Holland, M. M., J. L. Schramm, and J. A. Curry (1997), Thermodynamic feedback processes in a single-column sea-ice-ocean model, *Ann. Glaciol.*, **25**, 327–332.
- Holland, M. M., C. M. Bitz, and B. Tremblay (2006), Future abrupt reductions in the summer Arctic sea ice, *Geophys. Res. Lett.*, **33**, L23503, doi:10.1029/2006GL028024.
- Jin, Z. H., K. Stamnes, W. F. Weeks, and S. C. Tsay (1994), The effect of sea-ice on the solar-energy budget in the atmosphere sea-ice ocean system: A model study, *J. Geophys. Res.*, **99**, 25,281–25,294.
- Light, B., H. Eicken, G. A. Maykut, and T. C. Grenfell (1998), The effect of included particulates on the spectral albedo of sea ice, *J. Geophys. Res.*, **103**, 27,739–27,752.
- Light, B., G. A. Maykut, and T. C. Grenfell (2003a), A two-dimensional Monte Carlo model of radiative transfer in sea ice, *J. Geophys. Res.*, **108**(C7), 3219, doi:10.1029/2002JC001513.
- Light, B., G. A. Maykut, and T. C. Grenfell (2003b), Effects of temperature on the microstructure of first-year Arctic sea ice, *J. Geophys. Res.*, **108**(C2), 3051, doi:10.1029/2001JC000887.
- Light, B., G. A. Maykut, and T. C. Grenfell (2004), A temperature-dependent, structural-optical model of first-year sea ice, *J. Geophys. Res.*, **109**, C06013, doi:10.1029/2003JC002164.
- Maykut, G. A., and T. C. Grenfell (1975), Spectral distribution of light beneath 1st-year sea ice in the Arctic Ocean, *Limnol. Oceanogr.*, **20**, 554–563.
- Maykut, G. A., and N. Untersteiner (1971), Some results from a time dependent, thermodynamic model of sea ice, *J. Geophys. Res.*, **76**, 1550–1575.
- Mobley, C. D., G. F. Cota, T. C. Grenfell, R. A. Maffione, W. S. Pegau, and D. K. Perovich (1998), Modeling light propagation in sea ice, *IEEE Trans. Geosci. Remote Sens.*, **36**, 1743–1749.
- Moritz, R. E., and D. K. Perovich (1996), SHEBA: Science plan, *ARCSS OAH Manage. Off.*, 60 pp., Polar Sci. Cent., Univ. of Wash., Seattle.
- Parkinson, C. L., and D. J. Cavalieri (2002), A 21 year record of Arctic sea-ice extents and their regional, seasonal and monthly variability and trends, *Ann. Glaciol.*, **34**, 441–446.
- Parkinson, C. L., D. J. Cavalieri, P. Gloersen, H. J. Zwally, and J. C. Comiso (1999), Arctic sea ice extents, areas, and trends, 1978–1996, *J. Geophys. Res.*, **104**, 20,837–20,856.
- Pegau, W. S., and C. A. Paulson (2001), The albedo of Arctic leads in summer, *Ann. Glaciol.*, **33**, 221–224.
- Pegau, W. S., and J. R. V. Zaneveld (2000), Field measurements of in-ice radiance, *Cold Reg. Sci. Technol.*, **31**, 33–46.
- Perovich, D. K. (1990), Theoretical estimates of light-reflection and transmission by spatially complex and temporally varying sea ice covers, *J. Geophys. Res.*, **95**, 9557–9567.
- Perovich, D. K. (1991), Seasonal-changes in sea ice optical properties during fall freeze-up, *Cold Reg. Sci. Technol.*, **19**, 261–273.
- Perovich, D. K. (1994), Light-reflection from sea-ice during the onset of melt, *J. Geophys. Res.*, **99**, 3351–3359.
- Perovich, D. K. (2005), On the aggregate-scale partitioning of solar radiation in Arctic sea ice during the Surface Heat Budget of the Arctic Ocean (SHEBA) field experiment, *J. Geophys. Res.*, **110**, C03002, doi:10.1029/2004JC002512.
- Perovich, D. K., and T. C. Grenfell (1981), Laboratory studies of the optical-properties of young sea ice, *J. Glaciol.*, **27**, 331–346.
- Perovich, D. K., G. F. Cota, G. A. Maykut, and T. C. Grenfell (1993), Biooptical observations of 1st-year Arctic sea-ice, *Geophys. Res. Lett.*, **20**, 1059–1062.
- Perovich, D. K., C. S. Roesler, and W. S. Pegau (1998a), Variability in Arctic sea ice optical properties, *J. Geophys. Res.*, **103**, 1193–1208.
- Perovich, D. K., et al. (1998b), Field observations of the electromagnetic properties of first-year sea ice, *IEEE Trans. Geosci. Remote Sens.*, **36**, 1705–1715.
- Perovich, D. K., et al. (1999), Year on ice gives climate insights, *Eos Trans. AGU*, **80**, 481–486.
- Perovich, D. K., T. C. Grenfell, B. Light, and P. V. Hobbs (2002), Seasonal evolution of the albedo of multiyear Arctic sea ice, *J. Geophys. Res.*, **107**(C10), 8044, doi:10.1029/2000JC000438.
- Rothrock, D. A., Y. Yu, and G. A. Maykut (1999), Thinning of the Arctic sea-ice cover, *Geophys. Res. Lett.*, **26**, 3469–3472.
- Stroeve, J. C., M. C. Serreze, F. Fetterer, T. Arbetter, W. Meier, J. Maslanik, and K. Knowles (2005), Tracking the Arctic's shrinking ice cover: Another extreme September minimum in 2004, *Geophys. Res. Lett.*, **32**, L04501, doi:10.1029/2004GL021810.

- Untersteiner, N. (1961), On the mass and heat budget of Arctic sea ice, *Arch. Meteorol. Geophys. Bioklimatol., Ser. A*, 12(2), 151–182.
- Uttal, T., et al. (2002), Surface heat budget of the Arctic Ocean, *Bull. Am. Meteorol. Soc.*, 83, 255–275.
- van de Hulst, H. C. (1980), *Multiple Light Scattering Tables, Formulas, and Applications*, Academic, New York.
- Walsh, J. J., D. A. Dieterle, W. Maslowski, and T. E. Whitledge (2004), Decadal shifts in biophysical forcing of Arctic marine food webs: Numerical consequences, *J. Geophys. Res.*, 109, C05031, doi:10.1029/2003JC001945.
-
- T. C. Grenfell, Department of Atmospheric Sciences, University of Washington, Box 351640, Seattle, WA 98195, USA.
- B. Light, Applied Physics Laboratory, Polar Science Center, University of Washington, Seattle, WA 98105, USA. (bonnie@apl.washington.edu)
- D. K. Perovich, ERDC-CRREL, 72 Lyme Road, Hanover, NH 03755, USA.